Research Article Vol. 2, No. 9 / 15 Sep 2023 / *Optics Continuum* 1981

OPTICS CONTINUUM

Rapid scan white light pump–probe spectroscopy with 100 kHz shot-to-shot detection

VIVEK N. BHAT,[†] **ASHA S. THOMAS,**[†] **ATANDRITA BHATTACHARYYA, AND VIVEK TIWARI**[*]

Solid State and Structural Chemistry Unit, Indian Institute of Science, CV Raman Rd, Bengaluru, KA 560012, India

[†] The authors contributed equally to this work

[*] *vivektiwari@iisc.ac.in*

Abstract: We demonstrate a femtosecond pump–probe spectrometer that utilizes a white light supercontinuum as input and relies on mutual synchronization of the laser repetition rate, acousto-optical chopper, pump–probe delay stage, and the CCD camera to record shot-to-shot pump–probe spectra while the pump–probe delay is scanned synchronously with the laser repetition rate. The unique combination of technologies implemented here allows for electronically controllable and repetition-rate scalable detection throughput that is only limited by the camera frame rate. Despite high probe RMS fluctuations due to sample scatter (from ~1.8% with solvent to 7.9% with sample scatter), a combination of fast and slow averaging with a fine sampling of pump–probe delay leads to reduction of RMS noise without multichannel referencing down to ~0.4 mOD for a scattering nanotube sample. Throughput and limitations of the rapid versus stepwise scanning approaches are analyzed. Experimental comparison with stepwise scan shows ~1.9x noise reduction in a significantly faster experiment, suggesting an additional suppression of $1/f$ noise enabled by rapid scan data collection. The particular combination of technologies implemented here makes our approach especially suitable for high throughput impulsive pump–probe micro-spectroscopy of highly scattering samples, without added cost and complexity of light sources, multichannel detection, or long sample exposure.

1. Introduction

Ultrafast pump–probe spectroscopy has been instrumental in enabling mechanistic insights [1,2] into condensed phase ultrafast phenomenon ranging from femtosecond charge transfer reactions in solution, energy transfer in excitonically coupled systems such as photosynthetic proteins, and ultrafast exciton diffusion and dissociation in photovoltaic thin films. Although more sophisticated multidimensional spectroscopies [3,4] are available, the power of pump–probe lies in its relative ease of instrumentation and data processing. Pump–probe approaches have also been extended to nonlinear imaging [5,6] where the additional spatial information has allowed to disentangle the effects of sample morphology on electronic relaxation.

While typical pump–probe approaches use a narrowband pump and broadband supercontinuum probe, approaches based on a broadband pump provide enhanced time resolution and are particularly insightful [2] for inferring structural dynamics accompanying femtosecond internal conversion between electronic states. Broadband pump is typically generated through multi-stage optical parametric amplifiers [7–9] (OPAs) for reasons of significantly higher RMS stability [10,11] across the entire bandwidth and μJ pulse energies. Alternatively, a non-linear crystal based white light continuum (WLC) pump is relatively much easier to generate and therefore desirable to implement in pump–probe spectroscopy. However this imposes significant constraints of pulse energies of only a few nJ, with higher RMS fluctuations and spectral and temporal correlations

#496928 https://doi.org/10.1364/OPTCON.496928
Journal © 2023 Received 31 May 2023; accepted 22 Aug 2023; published 5 Sep 2023

[12] across the bandwidth. This necessitates either longer averaging times, or introducing multichannel referencing and balanced detection [10,12–14] to achieve desired signal-to-noise (SNR) levels. Alternatively, a few approaches [10] have implemented higher averaging through high-repetition rate shot-to-shot detection, which additionally leverages correlations between consecutive laser shots to suppress laser noise without the complexity of multichannel reference detection. For example, Grupp et al. [15] and Kanal et al. [16] have demonstrated shot-to-shot detection with stepwise scan of pump–probe delay T at 50 kHz and 100 kHz, respectively. Zanni and co-workers have demonstrated nearly octave-spanning WLC based two-dimensional electronic spectroscopy (2DES) [17]. 100 kHz shot-to-shot detection using acousto-optic pulse-shaping technology [18] suppresses $1/f$ experimental noise over the entire scan by fully leveraging correlations between laser shots. The additional suppression of $1/f$ experimental noise component transferred to the signal in the context of rapid scan pump–probe was also highlighted [19] by Moon et al. Rapid scanning T delay also achieves [19,20] better averaging through reduction in single scan time and therefore higher averaging. The above approaches demonstrate individual advantages of WLC based pump/probe light sources, shot-to-shot data collection, and rapid T scan. However, so far, pump–probe approaches that combine these advantages are scarce [10], with only limited capability in terms of repetition rate and T scan range. Development of WLC based pump–probe approaches which are repetition rate scalable, and provide efficient noise suppression while minimizing sample exposure, may be especially useful for broadband nonlinear micro-spectroscopy where a general impetus has been towards 1 MHz repetition rates [5,21] in order to compensate for small signal sizes resulting from picoJoule (pJ) pulse energies.

Here we combine the advantages of a broadband WLC source, high-repetition rate shot-to-shot detection and rapid T scanning to demonstrate white-light pump–probe spectroscopy of a scattering nanotube sample starting with only $\sim$ 1 nJ pump and probe pulse energies across the spectral bandwidth. Mutual synchronization of the laser repetition rate, acousto-optical chopper, delay stage and the CCD line camera enables a repetition-rate scalable and electronically tunable detection throughput that is only limited by the camera frame rate with the pump–probe delay scanned synchronously with the laser repetition rate. A noise floor down to $\sim$ 0.4 mOD is achieved after averaging over 20k laser shots along with effective suppression of spectral and temporal correlations [12] in the WLC. Throughput and limitations of stepwise versus rapid scanning are analyzed. Experimental comparison between the two approaches with equal number of samples shows ~2× reduction in noise with significantly faster scan time in case of rapid scanning, suggesting an additional $1/f$ noise suppression enabled by combining shot-to-shot detection with rapid T scanning. This demonstration finds promising applications in repetition rate scalable impulsive pump–probe micro-spectroscopy [6] of scattering samples with broadband spectral coverage and minimized sample exposure.

2. Experimental methods

2.1. Optical setup

The experimental setup schematic is shown in Fig. 1(A). Fundamental beam from a Yb:KGW amplifier (Spirit One, Spectra-Physics) at 100 kHz repetition rate, 1040 nm central wavelength and $\sim$ 300 fs full-width at half maxima (FWHM) pulse duration, is split into two arms each of $\sim$1 μJ pulse energy to generate pump and probe WLC. The pump and probe continua are generated by focusing a ~3 mm diameter input beam into 8 mm and 10 mm thick YAG crystals using 7.5 cm and 5 cm focal length lenses, respectively. The pump and probe continua are filtered using 725 nm and 850 nm shortpass filters (OD 4, Edmund Optics), respectively. The pump arm is then routed to a crystalline quartz acousto-optical deflector (AOD, Gooch and Housego model 97-02965-01) of optical pathlength 8.8 mm. The total dispersion in the pump arm, introduced by the YAG crystal, optical filters, AOD, focusing and collimating lenses, and the sample cuvette is partially pre-compensated by two pairs of group delay dispersion (GDD) oscillation compensated chirped mirrors (Layertec 148545, -40 fs^2 GDD per bounce) with total 38 pairs of bounces where each bounce pair is specified to compensate 1 mm of fused silica. Note that our placement of AOD after pump WLC generation introduces spatial chirp in the pump pulse. Reflective (achromatic) focusing with focal spotsizes substantially larger than ~1 μm are expected to mitigate the spatial chirp at the focus. However, measurements with sub-micron spatial resolution necessarily require either double-passing [22] through the AOD to exactly cancel out angular dispersion, or placement of AOD before pump WLC generation.

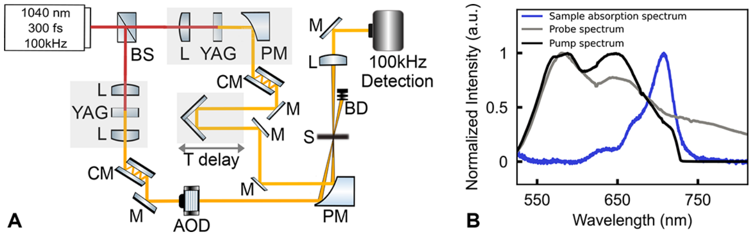

Fig. 1. (A) Experimental schematic of the rapid scan white light pump–probe spectrometer. BS, beam splitter; L, lens; CM, chirped mirror; M, mirror; AOD, acousto-optic deflector; PM, Parabolic mirror; S, Sample; BD, beam dump. 100KHz detection denotes the spectrograph, line camera and timing circuit that enables shot-to-shot detection. (B) Sample absorption spectrum overlaid with pump and probe spectra derived from the WLC.

The AOD is synced to the laser repetition rate f_R through a $f_R/2m$ TTL divider, where m corresponds to the number of consecutive pulses which are deflected/undeflected by the AOD. The deflected pulses are routed into the setup. m =1 corresponds to the case where every other pump pulse is blocked from exciting the sample. The probe arm is routed to a delay stage (ILS150BPP, Newport) and then to the sample with dispersion pre-compensation using a pair of GDD oscillation compensated chirped mirrors(Layertec 148545, -40 fs^2 GDD per bounce) with 22 bounce pairs. The pump and probe arms with parallel polarization are focused into a sample flowcell (pathlength 200 μm) using a parabolic mirror of focal length 101.6 mm. After the sample, the pump beam is blocked while the probe is routed to the spectrograph (iHR320 with 150 grooves/mm grating blazed at 500 nm, Horiba) using a combination of reflective optics and a 50 mm achromatic lens before the spectrograph. Every probe shot is recorded by a line CCD camera (e2v AViiVA, 14×28 μm 1024 pixels with Xtium-CL MX4 frame grabber 512 MB onboard memory buffer) attached to the spectrograph. Panel B shows the average pump and probe laser spectra measured at the sample location, and overlaid with the sample absorption spectrum. The pump laser bandwidth in the nearIR is shaped by the wavelength dependent AOD diffraction efficiency and the 725 nm shortpass filter. In this study we have used the pump bandwidth almost entirely, even though the overlap of the pump spectrum with the sample absorption spectrum is what determines [23] the pump excitation probability. Choosing only a selected region of pump bandwidth that maximizes this overlap is expected to enhance the SNR reported here by minimizing pump scatter contributions as well as potentially removing parts of pump WLC bandwidth with higher RMS fluctuations.

The pump and probe focal spot sizes at the sample location were measured to be ~43μm and ~41μm (Fig. S4) with pulse energies ~1.4 nJ and fluence of ~100 μJ/cm^2. The measured % transmission of both pump and probe, as well as the pump–probe signal, was confirmed to be linear with pump and probe power. Note that these pulse energies are over the entire pump and probe spectral bandwidth, where as excitation probability [23] depends on the overlap of fluence and absorption cross-section. This overlap is only a fraction of total WLC bandwidth for the case of nanotube sample as seen in Fig. 1(B). Furthermore, the exciton density was calculated [24] to be 1 per 153 molecules, which is significantly lower than the threshold at which non-linear effects arising from exciton-exciton interactions are expected (1 in 88 molecules [25]). We are also circulating the sample (Section 2.2). The above considerations suggest that probe induced non-linear effects are expected to be only minimal in our experiments even if the pump and probe pulse energies are chosen to be equal.

2.2. Sample preparation

The sample preparation details for the samples studied in Section 3.1 and Section 3.2 are briefly described below. Following previous protocols [25], 1mM meso-Tetra(4-sulfonatophenyl)porphine (TPP) dihydrochloride (Santa Cruz Biotechnology) in Ethanol was added to equal volume of 0.07N HCl/EtOH. Steady state absorption spectrum (Fig. 1(B)) confirmed the formation of porphyrin nanotubes. The sample (0.37 OD) is circulated through a flowcell (pathlength 200 μm) at a rate of ~102 ml/min using a peristaltic pump to ensure a fresh sample spot every 10μs, as well as to prevent the nanotubes from precipitating out of the solution. Oxazine 720 (Sigma-Aldrich) solution is prepared in methanol with OD 0.3 in 500 μm cuvette.

2.3. Data collection schemes

Figure 2(A) describes the timing electronics which is the crucial component of the experiment. The f_R = 100 kHz laser pulse train is converted to a TTL pulse train, which is then split into two signals. One part is converted to a $f_R/2$ TTL signal used to drive the RF controller of the AOD pump chopper. The second part is sent into an AND circuit along with a trigger signal from the T stage controller (Newport, XPS-D). The stage controller is set to output a high signal whenever the stage is within a defined T delay range, such that the AND gate triggers the CCD camera only within this defined stage trigger window. The camera reads every probe shot, with readout rate only limited by the camera line rate. Note that $m = 2$ or larger does not correspond to shot-to-shot detection but is electronically controllable in the above implementation, if so desired.

The shot-to-shot data collection scheme with rapid T scan is shown in Fig. 2(B). In the rapid T scan, stage velocity v and laser repetition rate f_R lead to a finely sampled T time step of $\delta T = (2m/f_R).(2v/c)$, where c is the speed of light in air. For the case of shot-to-shot detection ($m = 1$), consecutive probe shots with pump ON and OFF (gray shaded pulses) determine δT, and the corresponding pump–probe spectrum. In our study we have defined a frame as s =1000 consecutive probe shots and denoted as shaded blue in the figure. Each frame provides $s/2$ consecutive ON/OFF pairs, which are then averaged together to produce one binned time step ΔT, with total T_N binned time points as shown in the figure. Note that in the above scheme, the finely sampled time steps, both within a given frame as well as across frames, are scanned synchronously with the laser repetition rate. The scan starting point is then determined by the AND output of stage high trigger and the probe pulse train. In doing so, a timing error will be encountered due to the relative positions of stage high and 100 kHz TTL trigger. The maximum possible timing error is given by the maximum possible delay elapsed between stage high trigger and reading of the first probe shot, that is, ~ $(2v/f_R.c)$ where v is expressed in μm/μs and speed of light is assumed to be $c \approx 3 \times 10^8$ m/s. In our case, with f = 100 kHz and maximum stage velocity of 14.725 mm/s, this T timing error is ~ 1 fs. This error is expected to be substantial for a combination of low repetition rates and faster stage velocities. However, if desired, this can be easily corrected by independent and simultaneous measurement of pump–probe cross-correlation using a DAQ synchronized to the 100 kHz trigger.

Figure 2(C) shows the stage position profile recorded by the stage encoder as the stage moves from the set initial point with set acceleration to reach the defined constant velocity, followed by deceleration back to zero velocity. We define a distance d as the distance to be covered by the stage to accelerate to, or decelerate from, the set constant velocity. Based on the motion profile data gathered from the stage controller, the distance d can be experimentally determined as time taken by the stage to attain 99.8% of the set velocity. Once we determine d experimentally, we

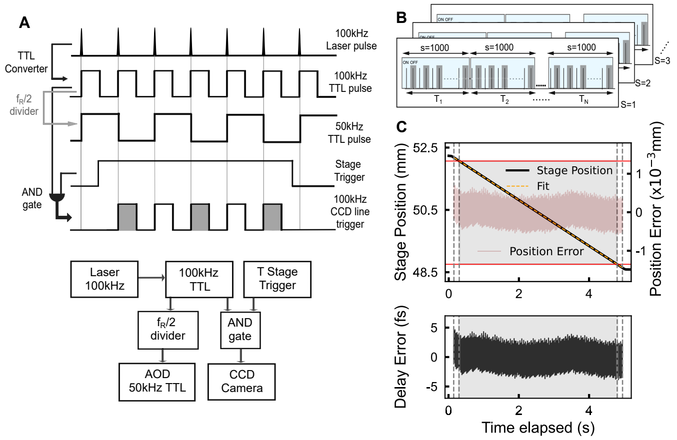

Fig. 2. (A) Timing diagram (top) and electronics synchronization scheme (bottom) showing the synchronization of laser repetition rate to AOD, CCD camera and stage trigger. Shaded region in the AND output represents the pump OFF state. (B) Shot-to-shot data acquisition and averaging scheme. S denotes a rapid scan over a defined T range, s denotes the number of probe spectra which are grouped together as one frame. Difference probe spectra between pump ON/OFF states defines a finely sampled step δT. $s/2$ such consecutive ON/OFF pairs are averaged together to lead to the binned time axis with stepsize ΔT. (C) Stage position versus time elapsed recorded by the stage encoder for a rapid T scan with the slowest velocity (Table 2). Motion profile of the stage (black solid line) and the corresponding fit (orange dashed line) with slope $0.736 \pm 4{\times}10^{-6}$ mm/s compared to the set velocity 0.736 mm/s. The light red band shows the residual position error. The corresponding residual delay error is shown in the bottom panel. The stage starts from rest to accelerate to the set velocity, or decelerate from it to go to rest. The extreme left and right vertical lines (gray dashed) indicate the time range in which the stage maintains 99.8% of set velocity. The stage trigger start and end points, which define the scan range (gray shaded region), are shown by the red horizontal lines, with corresponding time window mapped by the inner vertical lines.

allow the stage to move a total of $3d$ distance before and after the defined stage trigger window in order to ensure that the stage moves with uniform velocity within the trigger window during data acquisition. With an acceleration of 8 mm/s^2 and 0.736 mm/s velocity, the additional distance scanned is $3d \sim 0.168$ mm with corresponding elapsed time of 0.3 seconds. The effect of this additional time elapsed on rapid scan efficiency will be analyzed in Section 3.3. Note that the motion profile data in Fig. 2(C) corresponds to the case of the slowest velocity $v = 0.736$ mm/s (Table 2) employed in the experiments presented in Section 3.2, where the position errors are expected to be the largest. The extreme left and right vertical gray dashed lines show the time points at which the stage reaches 99.8% of the set velocity, respectively. The stage trigger start and end positions are indicated by the red horizontal lines, which define the scan range (gray shaded region) over which the probe shots are recorded by the CCD. The inner vertical lines map these positions to the time axis. The orange line is the best fit for the motion profile in the constant velocity region without constraining the slope to the set velocity. The slope of the best fit line is 0.736 mm/s (fitting error $4{\times}10^{-6}$ mm/s) compared to the set velocity of 0.736 mm/s. The residual position errors, shown as light red lines, are less than $\sim \pm 0.5$ μm, with corresponding timing errors (lower panel) of $\sim \pm 2.5$ fs compared to 50 fs binned stepsize ΔT.

For the rapid scan (RS) data collection scheme, for a desired binned time step ΔT, with $s/2$ consecutive ON/OFF pairs averaged together to constitute one binned time point T_N, the required stage velocity is accordingly set as $v = \frac{\Delta T}{s}.(f_{RC}/2)$. For instance, for a desired $\Delta T = 50$ fs with

$s = 1000$, the required $v = 0.736$ mm/s. With this set velocity, the maximum range scanned by the T delay stage, and therefore the maximum number of binned time points, is determined by the acquisition settings of the camera and frame grabber. For example, implementing a 'ring' acquisition mode in National Instruments IMAQdx [26] allows acquisition of images into frame grabber memory and processing of frames into the computer RAM in parallel. In contrast, a 'sequence' acquisition mode, as implemented here, enables acquisition of frames until the frame grabber memory is full and then dump them into the computer memory. In our case we are utilizing 88% of the full memory which corresponds to 432 frames, each with $s = 1000$ lines. The data reported in this paper correspond to the latter implementation such that the full delay range is divided into multiple ranges, and each successive range is scanned with an increasing ΔT step size. The stepsize in a given scan range is controlled by the set velocity for that range, with total 432 frames/range. Furthermore, in any given scan range, the sample is continuously exposed for only ~4.8 seconds before a mechanical shutter turns on to block the pump and probe beams. Each T scan range is first scanned S number of times until the desirable SNR is reached, before scanning the next range. Note that in this scheme each scan S is followed by ~12 seconds of dead time required to transfer the frames from frame grabber to the computer memory. This limitation arises due to a fixed frame grabber memory and will be present even in the step scan (SS) approach [16]. Note that a 'ring' acquisition mode can avoid the dead time limitation of the 'sequence' mode implemented here. However, the velocity profile will then need to be non-uniform in order to scan the full delay range without running into large file sizes with global data fitting issues.

In comparison, in case of the SS data collection scheme, we divide a given delay range into N samples, each denoted by a corresponding delay point T_i. Each delay point is averaged over $s = 1000$ laser shots. Thus, for a given T delay range to be scanned, in both approaches, SS or RS, the total number of laser shots over which a given time point T_i is averaged can be kept the same for a fair comparison. After collecting s shots at each time point, a combined waiting time w, to account for stage settling time and mechanical shutter time, is also added. These settings will be recalled later in Section 3.3 where the efficiency and limitations of RS and SS approaches are discussed.

3. Results and discussion

3.1. Noise analysis

Figure 3 presents the noise analysis of the experiment. Fig. 3(A) shows the probe spectrum passing through the solvent (blank) averaged over 20k consecutive laser shots. %RMS laser noise for all the wavelengths with blank (red) versus circulating nanotube sample (blue) are compared. The horizontal lines at 1.8% and 7.9% represent %RMS laser noise at the central wavelength of 665 nm for blank and scattering nanotube sample, respectively. The pump beam is blocked in these measurements. The ~4.4x increase in the probe RMS fluctuations suggests that sample scatter will dominantly contribute to noise in case of nanotube pump–probe experiments, whereas RMS fluctuations in the WLC will be the dominant contributor in case of molecules. Note that flow rate of the peristaltic pump and focal spot size will also influence the scatter contribution in case of the nanotube sample. Table 1 presents a comparison of relative errors arising from individual noise contributions in the experiment. It is seen that even when the dominant sample scatter contributions are excluded, RMS noise in the WLC dominates the shot-noise by ~8.5x.

Figure 3(B) (left) uses the 10^5 consecutive probe shots, for the case of scattering nanotube sample, to calculate [16] $\Delta\mathrm{OD} = \langle -\log_{10} \frac{C_{ON}}{C_{OFF}} \rangle$ for shot-to-shot ($m = 1$) and non shot-to-shot $m = 10, 100$ cases. As defined earlier, m is the number of consecutive probe shots (with pump ON and pump OFF) that are averaged together to obtain a pump–probe spectrum. M is the number of such spectra that are averaged together to obtain the final pump–probe spectrum at a given binned T time point. The number of probe shots $s = 2mM$ required to obtain these spectra

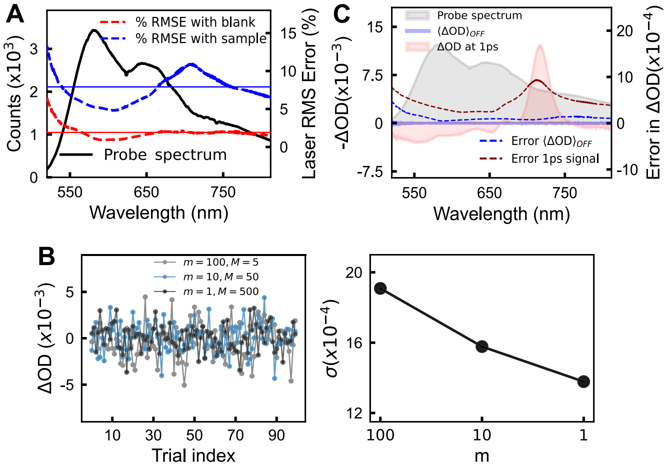

Fig. 3. (A) Averaged probe spectrum (black). %RMS error with a blank (solvent) and the nanotube sample is shown by red and blue dashed lines, respectively. The horizontal lines correspond to %error at 665nm. (B) (left) Effect of averaging schemes on the noise. ΔOD signal is calculated with sample present in the probe path and pump blocked. m denotes number of probe shots with pump ON/OFF, with $m = 1$ corresponding to shot-to-shot detection. Each set of ON/OFF probe shots leads to one pump–probe spectrum, which is then averaged over M such spectra. The total probe shots $s = 2mM$ used for each data point is kept fixed. (right) Standard deviation of the traces in the left panel. (C) Average ΔOD signal (solid line) along with the error (dashed line) calculated with the shot-to-shot detection scheme in panel B with total $S = 20$ T scans averaged together. This is identical to the averaging scheme used for the data presented in Fig. 5. Blue (blank) and red (nanotube sample) at $T = 1$ ps. Averaged probe spectrum (gray) is overlaid for reference.

Table 1. Comparison of relative errors from various noise contributions. $\overline{C}$ is measured at 665 nm. The estimation of relative error from electronic noise assumes the same number of averaged maximum photon counts as measured experimentally. The electronic readout noise of the line CCD camera is specified as 7.7 in terms of least significant bits (LSBs) or counts. 1 LSB represents 1 digital count after analog-to-digital conversion. Number of photons falling on the CCD camera, N_{Ph} is estimated [16] by first calculating the fraction of maximum average counts recorded on a given pixel, $\overline{C} = 2534$ and maximum possible counts for a 12-bit resolution, 4096. This fraction is multiplied by the CCD full well capacity to convert into photoelectrons. N_{Ph} is then obtained by taking into account that only a fraction of photons are converted into photoelectrons as dictated by the quantum efficiency of the sensor.

	Electronic Noise	Shot noise	Laser intensity fluctuation
mean value	$\overline{C} = 2534$ counts	$N_{Ph} = 2.16 \times 10^5$	$\overline{C} = 2534$ counts
noise	7.7 counts	$\sqrt{N_{Ph}} = 465.33$	46.37 counts
relative error	3.04×10^{-3}	$\frac{1}{\sqrt{N_{Ph}}} = 2.15 \times 10^{-3}$	18.28×10^{-3}

is kept fixed between these cases for a fair comparison. The standard deviation of ΔOD signal (Fig. 3(B), right), around the expected mean value of zero, is 13.8×10^{-4} for shot-to-shot scheme, which is ~1.14x and ~1.38x *lesser* than the non shot-to-shot $m = 10, 100$ schemes, respectively. This suggests that the advantages of shot-to-shot detection [16] are maintained even when sample scatter dominates the RMS probe noise (Fig. 3(A)).

Figure 3(C) calculates the average ΔOD signal for the case of $(m, M) = (1, 500)$, that is, shot-to-shot detection with $M = s/2$ consecutive ON/OFF pairs averaged at each T, and $S = 20$ T scans averaged. Note that this averaging scheme is identical to that employed for the pump–probe experiments presented later in Fig. 5. The ΔOD curve in case of the blank (solvent) is nearly flat over the entire probe bandwidth suggesting effective averaging of spectral and temporal WLC correlations [12]. Pump–probe signal in case of the nanotube sample at $T = 1$ ps is also included for comparison. The corresponding errors in ΔOD are shown as dashed lines. The average error in ΔOD over the entire spectral bandwidth is ~0.1 mOD and ~0.4 mOD for the blank and nanotube sample, respectively. As may be expected, higher RMS noise in the probe (Fig. 3(A)) carries over to the pump–probe signal, causing a higher ΔOD error in case of the scattering nanotube sample.

3.2. Rapid and stepwise pump–probe spectra

In this section, we compare the SNR of pump–probe T scans collected by RS and SS approaches with shot-to-shot data collection. In the SS case, T is scanned stepwise with a wait time of $w =$ 400 ms after each step, and stepsize of $\Delta T = 50$ fs. At each T point, the CCD camera captures a frame of s =1000 probe shots such that $M = 500$ consecutive ON/OFF pairs are averaged together to obtain data at each T step. One full T scan includes 200 different T points ranging from -750 fs to 9.25 ps and takes ~82 seconds including the stage settling time at each step. The data acquisition settings are kept as close as possible to those reported by Kanal et al. [16] for a stepwise shot-to-shot detection experiment on a laser dye at 100 kHz (200 T steps in 90 seconds with $M = 500$). For the case of nanotube sample, we fix the T delay range to be the *same* as SS case, with rapid scan time of ~4.4 seconds. This sets the velocity to 0.341mm/s and results in M =1080 consecutive ON/OFF pairs (2160 probe shots) per binned T step. However, as shown later, the same data can also be processed to only include $M = 500$ pairs for an equivalent comparison with the SS case. For the case of Oxazine 720 in Fig. 4(A), both RS and SS cases consider $(M, S) = (500,4)$. Note that smaller M implies that the set velocity (in RS case) can be set to be faster (0.736 mm/s), which in turn means that a *larger* T delay range (-750 fs to 20.85 ps) can be scanned in 4.4 seconds compared to the SS case, both with $\Delta T = 50$ fs.

Figure 4(A) compares the RS versus SS cases for Oxazine 720 in methanol for which minimal scatter contributions are expected (see Fig. 3(A),C). The exponential decay at 633 nm are overlaid for the two cases along with the fitting function. The decay constants obtained from the fitting are 0.12 ps, 1.19 ps and 74.68 ps with a 58 fs instrument response function (IRF), where the first two time constants are associated [27] with polar solvation and vibrational relaxation. Note that the validity of kinetic timescales reported in our pump–probe experiments depends on the IRF of the spectrometer. Accordingly Section 3.2 describes the determination of IRF using a global fit across all detection pixels with an assumed Gaussian IRF, which is a reasonable assumption made across several pump–probe studies. In Fig. 4(A), the RS data is shown in the same T range as the SS data. The residuals obtained after fitting the exponential decay are compared in the lower panel for a relatively flat T range of 2–9 ps. The standard deviations (σ) of the residuals are 4.56×10^{-3} and 5.17×10^{-3} for RS and SS respectively, suggesting only a marginal 1.15x improvement in the SNR of the scan for the RS case.

Figure 4(B) shows the exponential decay and corresponding fits at 718 nm for the porphyrin nanotube sample with RS and SS cases overlaid. The residuals for both cases are shown in the lower panel. The decay constants obtained from exponential fitting are 0.43 ps, 2.77 ps

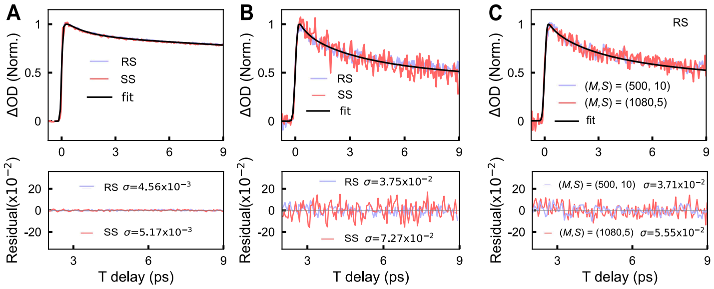

Fig. 4. Comparison of rapid scan (RS) and step scan(SS) approaches for shot-to-shot detection. The decay data are normalized by the maxima of the fit function and compared for RS and SS at the detection wavelength at which the signal is maximum. For all columns, the corresponding residual and the standard deviations are shown in the lower panels and compared on the same Y scale. (A) Oxazine 720 in methanol at 633 nm with number of consecutive *ON*/*OFF* pairs averaged, $M = 500$, and number of T scans, $S = 4$. (B) Porphyrin nanotubes in ethanol at 718 nm with $(M, S) = (1080, 10)$ for RS and $(M, S) = (500, 10)$ for SS. (C) A comparison of averaging over more number *ON*/*OFF* pairs per T (M) versus more number of T scans, S.

and 45.65 ps. The fitting function and the time constants are discussed in Section 3.2. The standard deviations σ for RS and SS cases are 3.75×10^{-2} and 7.27×10^{-2}, respectively, that is, ~1.9x higher SNR in a ~17x faster RS experiment. Note that the throughput gain in the RS approach depends on the stage settling time, shutter ON/OFF times at each T point, etc. which are instrumentation specific. For the stage and controller model in our experiment, stage settling times for a given stepsize can be improved down to ~100 ms. If the shutter ON/OFF times were ignored, the throughput gain is still ~4.6× along with SNR improvement of 1.9×. Note that this throughput argument ignores the fact that the step scan will always be fundamentally limited by settling times interleaved in between data collection, making it more susceptible to $1/f$ noise during [19] the T scan. Furthermore, efficiency estimations in Table 3 show that a rapid scan is still ~10× more efficient for the same fundamental reason. The point about efficiency is crucial because it directly impacts the $1/f$ experimental noise encountered during a T scan. It is also noteworthy that the overall SNR $(1/\sigma)$ is significantly poorer in the case of the scattering nanotube sample. This is evident from the residuals in the lower row which are all shown on the same Y-scale.

Figure 4(C) addresses the question whether averaging more number of *ON*/*OFF* pairs (M) per T step is more effective than averaging more number of scans (S). We consider the scan in panel B, where $(M, S) = (1080,10)$, but average only $S = 5$ T scans, that is, $(M, S) = (1080,5)$. Similarly, we average all the T scans (S =10) but average only M =500 pairs per binned T step, that is, $(M, S) = (500,10)$. Figure 4(C) overlays the RS data processed for the two cases with residuals and σ shown in the lower panel. As may be expected, for same number of T scans, S =10, averaging over more *ON*, *OFF* pairs, M =1080 versus 500, has little effect on the SNR of the scan, σ =3.75×10^{-2} versus 3.71×10^{-2}, respectively. This is so because larger M reduces standard error at a given T point but not the $1/f$ experimental noise encountered across the entire T scan. In contrast, while keeping $M = 1080$ fixed and averaging over more number of T scans, $S = 10$ versus 5, improves the SNR significantly, $\sigma = 3.75\times10^{-2}$ versus 5.55×10^{-2}. This outcome is in line with the approach implemented by Zanni and co-workers in case of WLC-based 2DES experiments where effective suppression of $1/f$ noise along the optical coherence time axis is reported. In their experiment the time axis is scanned by a programmable acousto-optic pulse shaper [18]. We term this approach as 'burst scan' which is the extreme case of rapid scan with $(m, M) = (1,1)$. Compared to current implementation of S scans with M *ON*/*OFF* pairs averaged per binned T step, this would be equivalent to $M \times S$ number of T scans instead. This is discussed further in Section 3.3.

Table 2 shows the three different stage velocities corresponding to the three T scan ranges R1–R3, in total spanning -0.75 ps to 650.88 ps. The corresponding binned stepsizes ΔT are also shown. Figure 5 extends the above RS approach to demonstrate pump–probe measurements on the porphyrin nanotube sample across multiple kinetic timescales. Figure 5(A) plots the pump–probe spectra for all T. Similar to analysis in Fig. 3, we have reported the pump–probe signal as ΔOD to be consistent with several prior reports [10], even though changes in probe photon number (ΔC) is what directly relates [23] to the pump–probe signal even if changes in absorption coefficient over the sample pathlength are not small. During setup alignment any trends in the probe focal spot misaligning on the line CCD array due to T stage movement were checked carefully. Briefly, we first measure the power transmitted through the 5 μm pinhole at the focus. The change in %transmitted power with stage movement is $< 1\%$ (Fig. S1). We also cross verify the probe alignment on the CCD line array by scanning the stage over the entire T range. The maximum % change in counts over the entire spectrum is 4.2% (Fig. S2). Any stage velocity dependent misalignment on the CCD line array was ruled out by scanning the stage with three different velocities, but in a common scan range. The probe spectra measured at different velocities show a variation of 0.48% (Fig. S3). All these alignment variations are within the 7.9% RMS error in the transmitted probe spectrum (Fig. 3(A)) in the presence of the nanotube sample. Note that the ΔOD pump–probe signal depends on the ratio of probe counts falling on the CCD line array with pump *ON* and *OFF*. Therefore ΔOD at any T is intrinsically insensitive to minor variations in probe counts registered by the CCD sensor. Further, overlapping scan ranges between R1–R2 and R2–R3 (Table 2) were chosen to cross check and correct for any residual minor deviations, if any, during data processing. In the data, any deviations in ΔOD between scan ranges were smaller than the ΔOD error bar and no such correction was required. 20 frames at −5 ps are averaged and used to remove the scatter background from the data. Note that perpendicularly polarized probe with a corresponding analyzer before the spectrograph can also help with pump scatter suppression, especially for 2DES experiments [28]. However this configuration also limits pump–probe polarization anisotropy experiments if desired. Instead for pump–probe experiments, a separate measurement of pump scatter background works reasonably well to remove the scatter background. The scatter removed pump–probe data (Fig. 5(A)) is globally fitted in the GloTarAn [29] software to a multi-exponential decay. This can be represented [30] as $\Psi(T,\lambda) = \sum_i (\exp(-k_i T) \otimes IRF) A_i(\lambda)$ where Ψ is the measured pump–probe signal in ΔOD, i represents the exponential decay index, $A_i(\lambda)$ is the corresponding amplitude as a function of wavelength, and $\otimes$ represents the convolution with a Gaussian IRF. The *IRF* is given by $IRF(T) = \frac{\sqrt{(8\ln 2)}}{\sqrt{(2\pi\Delta^2)}} \exp(-\ln 2[\frac{2(T-\mu)}{\Delta}]^2)$ where Δ is the FWHM and μ is the center, and represents a cross-correlation of the pump and probe. For a chirped supercontinuum probe, the IRF approximately reflects [31] the pump pulse duration. Due to residual uncompensated probe chirp, μ depends on λ and the dependence is described as a third-order polynomial fit for probe chirp correction [32]. The decay of signal maxima (718 nm) is shown in Fig. 5(B). An IRF of ~58 fs is obtained from a global fit of the data and suggests uncompensated higher-order dispersion in the pump caused by limitations in our pulse compression which only relies on chirped mirrors. Accordingly no timescale of the order of IRF is claimed in this study. Note that the transients recorded in a pump–probe experiment are insensitive to residual phase on the pump pulses. Hence uncompensated dispersion in the pump pulses does not affect the central theme of the shot-to-shot rapid scan pump–probe approach presented here.

Global fit of the data yields four exponential decay constants – 0.43 (0.01) ps, 2.77 (0.05) ps, 26.45 (0.13) ps and 1.16 (0.01) ns, where the respective fitting errors are shown in parenthesis. The spectral features and time constants porphyrin nanotubes are in good agreement with the

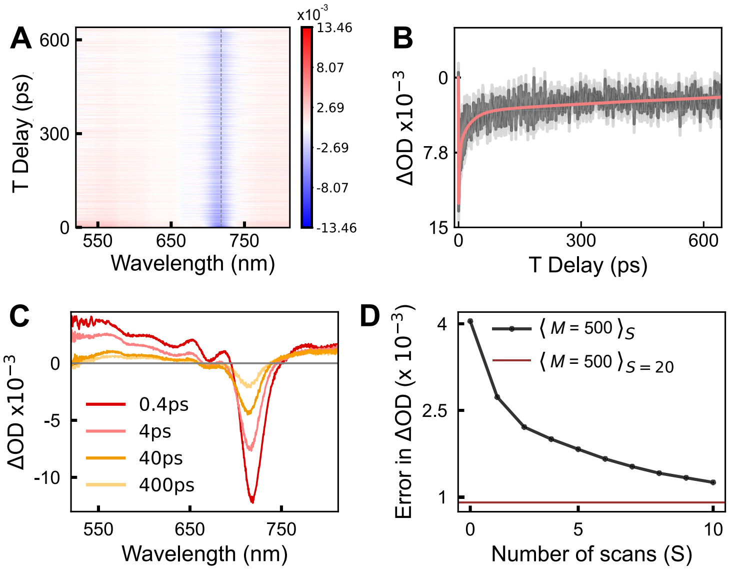

Fig. 5. (A) 2D contour plot of ΔOD pump–probe spectra of porphyrin nanotubes versus T for (M, S) = (500,20). The vertical line corresponds to 718 nm slice shown in panel B. (B) ΔOD signal decay (dark gray) at 718 nm overlaid with the error bar (light gray) and the global fit (orange) of the data in panel A. (C) Pump–probe spectra at selected T delays obtained as horizontal slices of panel A. (D) Error in ΔOD signal at T = 1 ps and 718 nm, where each point denotes error after averaging the first S scans. The horizontal line indicates the final error bar of ± 0.9 mOD after S = 20 scans.

Table 2. Details of shot-to-shot rapid scan parameters. (m, M, S) = (1,500,20) for all the ranges scanned.

Range	Velocity (mm/s)	ΔT (fs)	scan range (ps)
R1	0.736	50	-0.75 to 20.85
R2	7.362	500	14.85 to 230.86
R3	14.725	1000	218.86 to 650.88

reported [25,33] literature. The faster timescale is reported [33] as intra-Q band electronic relaxation, and 2.77 ps and 26.45 ps timescales are attributed [33] to vibrational relaxation. A longest decay component of 1.16 ns was necessary to fit the slowly decaying component [25]. This time constant can be attributed to the Q-band population lifetime although with low certainty due to scan range being limited to ~0.7 ns. Pump–probe spectra at different T across the entire delay range are shown in Fig. 5(C). The prominent negative ΔOD signal at 718 nm corresponds to the Q_x bleach, while the Q_y bleach at 670 nm overlaps with the dominant broad excited state absorption background [33]. Figure 5(D) shows the error in the measured ΔOD signal at 718 nm and 1 ps T delay after averaging first S scans. The horizontal line indicates the final error bar of ± 0.9 mOD after S =20 scans with the expected $1/\sqrt{S}$ dependence.

3.3. Rapid versus stepwise scanning—limitations and throughput

Below we analyze the throughput limitations of the RS approach for shot-to-shot pump–probe spectroscopy demonstrated in Section 3.2. We also compare this technique to the SS approach in terms of experimental efficiency, and suggest situations where the RS approach may be particularly effective.

For the sake of simple analytic comparisons, we will consider a mono-exponential signal with time constant τ that is to be sampled in an experiment until E time constants. The total delay range becomes $E\tau$ such that the total time range to be sampled by the stage becomes $E\tau/2$. We will assume the constraint of a minimum of $p = s/2$ samples, where s is the number of probe shots and the samples are separated by stepsize δT (Section 2.3). We denote the stage velocity as v (μm/sec) and assume speed of light in air to be $c \sim 3 \times 10^8$ (m/s). We will assume a 'sequence' mode scan where the total number of probe shots N_T collected by the CCD line camera are limited by the frame grabber memory. Our estimation of scan efficiency discussed below does not consider the limitation of dead time encountered at the end of a given T scan, which arises in 'sequence' mode due to a limited frame grabber memory, because this limitation is common to both, RS and SS approaches. Furthermore, dead time after a T scan has no bearing on the $1/f$ noise encountered during a T scan, which is the key difference between the RS and SS approaches. Using these parameters, we can now derive upper and lower bounds on the stage velocity v required for sampling the delay range $E\tau$ into p samples. For stage velocity v, the time delay is scanned at a rate of $\frac{20v}{3} \times 10^{-6}$ fs/μs. For a shot-to-shot pump–probe step size of $2/f_R$ (μs), the step size δT (fs) (Section 2.3) becomes $\frac{40v}{3f_R} \times 10^{-6}$. Equating this step size to $E\tau/p$, the maximum possible stage velocity that still ensures p samples is given by $v_{max} = \frac{3}{40}(\frac{E\tau}{p})f_R \times 10^6$ (μm/s). Along the same lines, the minimum stage velocity required to ensure that the delay range $E\tau$ is scanned within N_T probe shots can be written as $v_{min} = \frac{3}{20}.(E\tau).(\frac{f_R}{N_T})$ (μm/s). Thus, in terms of experimental throughput when scanning a given T range with shot-to-shot detection, the maximum possible stage velocity v_{max} scales proportionally with the repetition rate f_R. Conversely, a minimum stage velocity is always required to be able to sample a given delay range within the frame grabber memory because δT delay steps get shorter with increasing f_R. The key difference between the two limits is that in case of the maximum possible velocity, one ON/OFF pair directly leads to time step ΔT, that is, there is no binning and averaging of consecutive ON/OFF pairs (M =1). This is akin to a 'burst scan' [18] where there is no binning of consecutive ON/OFF pairs but equivalently more number of time scans (Section 3.2). Burst scan is quite effective with a programmable pulse shaper [18] with no mechanical elements, although with a limited scan range. In case of a mechanical delay stage, as implemented here and more suited for typically large T delays, $M \times S = 500 \times 20$, T burst scans can be unfeasible. Crucially, stage movement during pump ON/OFF states cannot be ignored in burst scan and is one of the limitations of rapid scan approaches in general [34]. As opposed to a burst scan, Engel and co-workers have demonstrated that binning finely sampled consecutive ON/OFF pairs [35] can be quite effective in averaging dominant scatter contributions from photosynthetic cells in 2DES.

After describing the velocity bounds for a RS experiment, we can now compare the efficiency of this approach compared to the SS approach in order to judge the experimental regime most suitable for the two approaches. We will start by defining efficiency of a given delay scan as $\eta = \frac{1}{1+W/U}$, where W and U correspond to the number of probe shots wasted and utilized for data collection during a given scan. For a given scan S, we consider a scan with total N T points evenly distributed in the delay range $E\tau$. Additionally, in line with reported experiments, we consider total M consecutive ON/OFF pairs that are averaged together at each T point. Thus total probe shots utilized for the entire scan is $U^{ss} = 2MN$, where the superscript 'ss' denotes step scan. In a step scan, the stage waiting time w^{ss} (in seconds) is interleaved in between data collection steps. Therefore, the number of wasted pulse during a scan can be written as $W^{ss} = N.w^{ss}.f_R$. Therefore, efficiency becomes $\eta^{ss} = \frac{1}{1+f_R.w^{ss}/2M}$.

In case of RS, stage wait times are not interleaved in between data collection. However, as shown in Fig. 2(C), for a given scan S, a minimum distance d (μm) is needed in order for the stage to attain a constant velocity within the defined delay range. This additional distance contributes to wasted pulses W^{rs}, where the superscript denotes rapid scan. Input parameters for the stage motion profile such as final set velocity v and stage acceleration a determine the distance covered by the stage before attaining a constant velocity, or coming to a halt from constant velocity. In the experiments we set d to be thrice this distance and on either side of the constant velocity profile. For the analysis of experimental efficiency, we assume the scenario where the entire distance $3d$ is covered at the constant stage velocity. The time it takes to cover the additional distance $3d$ on either side of the data collection window (Fig. 2(C)) is then given by $2 \times 3d/v$ such that $W^{rs} = (\frac{3d}{v})2f_R$. Similar to the SS case, we consider total N samples with total $2M$ probe shots contributing to one sample, such that $U^{rs} = 2MN$. That is, the number of utilized pulses is kept the same between the two approaches for a fair comparison. We can then determine the stage velocity v_{max} that allows total $2MN$ probe shots within the stage scan range of $E\tau/2$, with $v_{max} = \frac{3}{40}(\frac{E\tau}{MN})f_R \times 10^6$ μm/s. Using v_{max}, W^{rs} can be simplified as $W^{rs} = 12\frac{dMN}{E\tau}\frac{20}{3}$. Thus, the efficiency of a rapid scan can be expressed as $\eta^{rs} = \frac{1}{1+\frac{3d(20/3)}{E\tau/2}}$.

Overall, a comparison of η^{ss} and η^{rs} suggests that η^{ss} scales inversely with the laser repetition rate f_R, that is, SS approach becomes less efficient at high repetition rates desirable for microspectroscopy experiments. Alternatively, for a fixed repetition rate, RS becomes more efficient with increasing delay range $E\tau$. Furthermore, for a fixed number of samples and delay range, RS can be made more efficient by minimizing the distance d before the stage attains constant velocity. The time elapsed in attaining a constant velocity is limited by the stage acceleration but is dominated by our setting of 3× this distance before data acquisition is triggered. In comparison, SS efficiency is ultimately limited by the stage settling time *interleaved* between delay points, which cannot be made arbitrarily small. This fundamental limitation of SS approach is evident from the efficiency estimation for the experiments in Fig. 4 presented in Table 3. Note that in the above comparison the ~10× higher efficiency of RS directly relates to the suppression of $1/f$ experimental noise encountered during [19] a T scan. Such a suppression also confers additional advantages to RS especially for experiments where coherent dynamics along the waiting time T is of interest. For example, a recent 2DES approach with fluorescence-detection has employed a rapid T scan approach to report [27] vibrational coherences at optical densities ~3 orders of magnitude below conventional approaches.

Table 3. Efficiency estimation for a RS and SS scan presented in Fig. 4. Total number of utilized pulses between both experiments is fixed such that $U^{ss} = U^{rs} = 200\text{E}3$ for total 200 samples. The efficiency is estimated using the expression $\eta = 1/(1 + W/U)$. For the SS approach, optimized stage settling times down to 100 ms (Section 3.2) are also included in the efficiency estimation. For the RS approach, 3*d* and *d* refers to the additional distance traveled by the stage before the data collection window starts (Fig. 2). From the encoder data in Fig. 2(C), the stage takes 0.147s to travel from start to *d* and attain constant velocity, and 0.152s to travel from *d* to 3*d* at the set constant velocity. Calculation of η^{rs} includes this extra time on either side of the data collection window (Fig. 2(C)).

SS	w^{ss} = 0.4s per T step	w^{ss} = 0.1s per T step
W^{ss}	8E6	2E6
% η^{ss}	2.4	9.1

RS	$3d$	d
W^{rs}	59.8E3	29.4E3
% η^{rs}	77	87

4. Conclusions

We have presented a repetition-rate scalable approach for shot-to-shot rapid scan white-light pump–probe spectroscopy. Mutual synchronization of the laser repetition rate, acousto-optical chopper, delay stage and the CCD line camera allows sampling of T delay synchronously with the laser repetition rate. Challenges associated with a white light continuum such as limited pulse energies and spectral and temporal instabilities, and with high probe RMS fluctuations (7.9%) due to sample scatter are effectively mitigated by a combination of fast and slow averaging schemes with fine sampling of pump–probe delay. Compared to a step scan approach, the rapid scan approach provides a 1.9× noise reduction in a significantly faster experiment with effective suppression of $1/f$ experimental noise over the T scan. Comparison of limitations and efficiency of the two approaches suggests advantages of rapid scan shot-to-shot detection in high-repetition-rate impulsive pump–probe microscopy experiments where coherent early T dynamics is expected, or in pump–probe experiments where large delay scans are typical. The approach demonstrated here provides a promising path towards high-throughput white-light pump–probe microscopy of scatter prone samples with minimized sample exposure.

Funding. Indian Space Research Organisation (ISTC/CSS/VT/468); Department of Biotechnology, Ministry of Science and Technology, India (BT/PR38464/BRB/10/1893/2020); Board of Research in Nuclear Sciences (58/20/31/2019-BRNS); Science and Engineering Research Board (CRG/2019/003691, CRG/2022/004523).

Acknowledgments. VNB acknowledges research fellowship from DST-Inspire. AST and AB acknowledge Prime Minister's Research Fellowship, MoE India.

Disclosures. The authors declare no conflicts of interest.

Data availability. Data underlying the results presented in this paper are not publicly available at this time but may be obtained from the authors upon reasonable request.

Supplemental document. See Supplement 1 for supporting content.

References

1. M. Maiuri, M. Garavelli, and G. Cerullo, "Ultrafast spectroscopy: state of the art and open challenges," J. Am. Chem. Soc. **142**(1), 3–15 (2020).
2. M. Liebel, C. Schnedermann, T. Wende, and P. Kukura, "Principles and applications of broadband impulsive vibrational spectroscopy," J. Phys. Chem. A **119**(36), 9506–9517 (2015).
3. F. D. Fuller and J. P. Ogilvie, "Experimental implementations of two-dimensional Fourier transform electronic spectroscopy," Annu. Rev. Phys. Chem. **66**(1), 667–690 (2015).
4. V. Tiwari, "Multidimensional electronic spectroscopy in high-definition—combining spectral, temporal and spatial resolutions," The J. Chem. Phys. **154**(23), 230901 (2021).
5. M. C. Fischer, J. W. Wilson, F. E. Robles, and W. S. Warren, "Invited review article: pump–probe microscopy," Rev. Sci. Instrum. **87**(3), 31101 (2016).
6. G. Piland and E. M. Grumstrup, "High-repetition rate broadband pump–probe microscopy," J. Phys. Chem. A **123**(40), 8709–8716 (2019).
7. G. Cirmi, C. Manzoni, D. Brida, S. D. Silvestri, and G. Cerullo, "Carrier-envelope phase stable, few-optical-cycle pulses tunable from visible to near IR," J. Opt. Soc. Am. B **25**(7), B62–B69 (2008).
8. D. Herrmann, C. Homann, R. Tautz, M. Scharrer, P. S. Russell, F. Krausz, L. Veisz, and E. Riedle, "Approaching the full octave: noncollinear optical parametric chirped pulse amplification with two-color pumping," Opt. Express **18**(18), 18752–18762 (2010).
9. A. Baltuška, T. Fuji, and T. Kobayashi, "Visible pulse compression to 4 fs by optical parametric amplification and programmable dispersion control," Opt. Lett. **27**(5), 306–308 (2002).
10. B. Lang, "Photometrics of ultrafast and fast broadband electronic transient absorption spectroscopy: state of the art," Rev. Sci. Instrum. **89**(9), 93112 (2018).
11. M. Bradler, P. Baum, and E. Riedle, "Femtosecond continuum generation in bulk laser host materials with sub-μJ pump pulses," Appl. Phys. B **97**(3), 561–574 (2009).
12. M. Bradler and E. Riedle, "Temporal and spectral correlations in bulk continua and improved use in transient spectroscopy," J. Opt. Soc. Am. B **31**(7), 1465–1475 (2014).
13. A. L. Dobryakov, S. A. Kovalenko, A. Weigel, J. L. Pérez-Lustres, J. Lange, A. Müller, and N. P. Ernsting, "Femtosecond pump/supercontinuum-probe spectroscopy: optimized setup and signal analysis for single-shot spectral referencing," Rev. Sci. Instrum. **81**(11), 113106 (2010).
14. J. Brazard, L. A. Bizimana, and D. B. Turner, "Accurate convergence of transient-absorption spectra using pulsed lasers," Rev. Sci. Instrum. **86**(5), 53106 (2015).
15. A. Grupp, A. Budweg, M. P. Fischer, J. Allerbeck, G. Soavi, A. Leitenstorfer, and D. Brida, "Broadly tunable ultrafast pump–probe system operating at multi-kHz repetition rate," J. Opt. **20**(1), 014005 (2018).
16. F. Kanal, S. Keiber, R. Eck, and T. Brixner, "100-kHz shot-to-shot broadband data acquisition for high-repetition-rate pump–probe spectroscopy," Opt. Express **22**(14), 16965–16975 (2014).

17. R. D. Mehlenbacher, T. J. McDonough, M. Grechko, M.-Y. Wu, M. S. Arnold, and M. T. Zanni, "Energy transfer pathways in semiconducting carbon nanotubes revealed using two-dimensional white-light spectroscopy," Nat. Commun. **6**(1), 6732 (2015).
18. N. M. Kearns, R. D. Mehlenbacher, A. C. Jones, and M. T. Zanni, "Broadband 2D electronic spectrometer using white light and pulse shaping: noise and signal evaluation at 1 and 100 kHz," Opt. Express **25**(7), 7869–7883 (2017).
19. J. A. Moon, "Optimization of signal-to-noise ratios in pump–probe spectroscopy," Rev. Sci. Instrum. **64**(7), 1775–1778 (1993).
20. J. W. Wilson and R. A. Bartels, "Rapid birefringent delay scanning for coherent multiphoton impulsive Raman pump–probe spectroscopy," IEEE J. Sel. Top. Quantum Electron. **18**(1), 130–139 (2012).
21. G. Donnert, C. Eggeling, and S. W. Hell, "Major signal increase in fluorescence microscopy through dark-state relaxation," Nat. Methods **4**(1), 81–86 (2007).
22. E. A. Donley, T. P. Heavner, F. Levi, M. O. Tataw, and S. R. Jefferts, "Double-pass acousto-optic modulator system," Rev. Sci. Instrum. **76**(6), 063112 (2005).
23. B. Cho, V. Tiwari, R. J. Hill, W. K. Peters, T. L. Courtney, A. P. Spencer, and D. M. Jonas, "Absolute measurement of femtosecond pump–probe signal strength," J. Phys. Chem. A **117**(29), 6332–6345 (2013).
24. B. Kriete, J. Lüttig, T. Kunsel, P. Malý, T. L. C. Jansen, J. Knoester, T. Brixner, and M. S. Pshenichnikov, "Interplay between structural hierarchy and exciton diffusion in artificial light harvesting," Nat. Commun. **10**, 4615 (2019).
25. Y. Wan, A. Stradomska, S. Fong, Z. Guo, R. D. Schaller, G. P. Wiederrecht, J. Knoester, and L. Huang, "Exciton level structure and dynamics in tubular porphyrin aggregates," J. Phys. Chem. C **118**(43), 24854–24865 (2014).
26. "National Instruments IMAQdx," *https://www.ni.com/docs/en-US/bundle/ni-imaqdx-vi-ref/page/ni-imaqdx_vi_reference/ni-imaqdx_pal.html*.
27. A. Sahu, V. N. Bhat, S. Patra, and V. Tiwari, "High-sensitivity fluorescence-detected multidimensional electronic spectroscopy through continuous pump–probe delay scan," The J. Chem. Phys. **158**(2), 24201 (2023).
28. A. C. Jones, N. M. Kearns, J.-J. Ho, J. T. Flach, and M. T. Zanni, "Impact of non-equilibrium molecular packings on singlet fission in microcrystals observed using 2D white-light microscopy," Nat. Chem. **12**(1), 40–47 (2020).
29. J. J. Snellenburg, S. P. Laptenok, R. Seger, K. M. Mullen, and I. H. M. van Stokkum, "Glotaran: a Java-based graphical user interface for the R-package TIMP," J. Stat. Soft. **49**(3), 1–22 (2012).
30. I. H. M. van Stokkum, D. S. Larsen, and R. van Grondelle, "Global and target analysis of time-resolved spectra," Biochimica et Biophysica Acta (BBA) - Bioenergetics **1657**(2-3), 82–104 (2004).
31. S. A. Kovalenko, A. L. Dobryakov, J. Ruthmann, and N. P. Ernsting, "Femtosecond spectroscopy of condensed phases with chirped supercontinuum probing," Phys. Rev. A **59**(3), 2369–2384 (1999).
32. P. F. Tekavec, J. A. Myers, K. L. M. Lewis, and J. P. Ogilvie, "Two-dimensional electronic spectroscopy with a continuum probe," Opt. Lett. **34**(9), 1390–1392 (2009).
33. H. Kano and T. Kobayashi, "Time-resolved fluorescence and absorption spectroscopies of porphyrin J-aggregates," The J. Chem. Phys. **116**(1), 184–195 (2002).
34. Z. W. Fox, T. J. Blair, R. B. Weakly, T. L. Courtney, and M. Khalil, "Implementation of continuous fast scanning detection in femtosecond Fourier-transform two-dimensional vibrational-electronic spectroscopy to decrease data acquisition time," Rev. Sci. Instrum. **89**(11), 113104 (2018).
35. P. D. Dahlberg, P.-C. Ting, S. C. Massey, M. A. Allodi, E. C. Martin, C. N. Hunter, and G. S. Engel, "Mapping the ultrafast flow of harvested solar energy in living photosynthetic cells," Nat. Commun. **8**(1), 988–994 (2017).